A phosphine oxide route to formamidinium lead tribromide nanoparticles

Olivia J. Ashton, Ashley R. Marshall, Jonathan H. Warby, Bernard Wenger, Henry J. Snaith**

Clarendon Laboratory, Department of Physics, University of Oxford, Parks Road, OX1 3PU, Oxford, UK

Abstract We present the synthesis of formamidinium lead tribromide ($FAPbBr_3$) perovskite nanocrystals through a phosphine oxide route, where, in comparison to more traditional syntheses, oleylamine is replaced with trioctylphosphine oxide (TOPO). This route has previously been shown to be successful for the inorganic cesium lead tribromide perovskite nanocrystals. We examine the interactions between the precursors via nuclear magnetic resonance spectroscopy (NMR). We confirm the existence of an interaction between FA-oleate and TOPO and use this to guide the optimisation of our synthesis. When the reaction is conducted at room temperature, we observe the formation of nanoparticles with high photoluminescence quantum yield (PLQY, ~70 %) at 2.39 eV (518 nm) with little ripening or size defocusing over time. Although we obtain narrow emission peaks, the crystals are irregular in shape, testament to the impact of the FA-oleate:TOPO interaction. Despite a drop in PLQY in the washed solutions, films made maintain a high PLQY of ~ 50 % at 2.33 eV (532 nm), which is fortuitously the ideal wavelength for the green emission channel in displays, and we demonstrate 532 nm electroluminescence in light emitting diodes with an EQE of 3.7 %.

Introduction

There are two popular routes to synthesize lead halide perovskite nanocrystals: ligand assisted reprecipitation[1–9] (LARP) and hot injection.[10–15] The most common ligands used in both methods are oleic acid (OA) and oleylamine (OLAm), which form a complex ligand shell of oleylammonium and oleate in equilibrium with one another and other species in solution.[16] Hot injection is generally favoured in semiconductor nanocrystal synthesis for controlling the size of the nanocrystals and achieving narrow size distributions,[17–21] which has been demonstrated for cesium lead halide, $CsPbX_3$, nanocrystals.[10,22] It is a two-precursor approach, with Cs-oleate being injected into a solution of lead halide with OA and OLAm in 1-octadecene (ODE).

Formamidinium ($CH(NH_2)_2^+$, FA) is an organic cation, which is currently used in most high efficiency perovskite thin film photovoltaic devices. To date, $FAPbX_3$ nanocrystals have been synthesised both via LARP or hot injection.[11,12,23,24] For the hot injection route, a modified three-precursor approach was required to form monodisperse nanocrystals, employing lead acetate, formamidinium acetate and oleylammonium halide,[11] as opposed to the two-precursor approach using lead halide and formamidinium oleate (FA-oleate). In the latter case when FA-oleate was used, polydisperse nanoparticles with inferior optical properties, such as larger full width half maxima in their photoluminescence or multiple photoluminescence peaks, were obtained. This was speculatively attributed to an unfavourable interaction of FA and OLAm, which had to be regulated by introducing oleylammonium bromide.[11,12]

Instead of trying to control the interaction between FA and OLAm during the synthesis, an alternative route is to remove the amine/ammonium ligand system altogether. $CsPbBr_3$ nanocrystals have been synthesised via an injection route with trioctylphosphine oxide (TOPO), without employing amine/ammonium molecules, [25] which produced oleate-only capped perovskite nanocrystals. This previous work, aimed at simplifying the dynamic oleate-oleylammonium ligand shell, also investigated

the relationship between TOPO and oleic acid (OA), and produced highly luminescent, monodisperse nanocrystals in record yields.

The success of the phosphine oxide route in the synthesis of $CsPbBr_3$ nanocrystals is attributed to the manipulation of the acid-base interaction of OA and TOPO.[25] In $CsPbBr_3$ synthesis, the reaction mixture consists of $PbBr_2$ dissolved by TOPO in 1-octadecene with some OA present. Upon the injection of Cs-oleate in OA, TOPO preferentially interacts with the excess OA, thus releasing $PbBr_2$ which reacts with Cs-oleate. This forms monodisperse $CsPbBr_3$ nanocrystals in reaction yields close to the theoretical limit.

Proton (^{1}H) nuclear magnetic resonance spectroscopy (NMR) has been used extensively to examine the ligand shell surrounding lead halide perovskite nanocrystals and the ligand-ligand interactions in solution,[16,25–27] but these studies are usually restricted to $CsPbX_3$ nanocrystals. The ^{1}H NMR signal of hydrogen atoms bound to amines shift drastically as a function of concentration and solvent polarity due to hydrogen bonding. Mixing amidinium and ammonium moieties makes it difficult to distinguish and interpret the signals from these moieties, due to their similar peak shifts and hydrogen bonding in solution.

Here, we investigate the impact of the A-site cation (FA^+) on the acid-base equilibrium of the ligands (OA and TOPO) using ^{1}H and ^{31}P NMR and then apply the phosphine oxide synthesis route to $FAPbBr_3$ nanocrystals. This synthesis has the potential to produce high quality $FAPBr_3$ nanocrystals in high yields, at low temperatures, with an oleate-only ligand shell by completely removing the amine/ammonium ligand species from the reaction; mitigating any FA/ligand interactions.

Table 1 NMR solutions with given concentrations in d-toluene

Sample	[TOPO] M	[OA] M	[A-oleate] M
TOPO	0.43	0.00	0.00
OA	0.00	0.53	0.00
OA:TOPO	0.43	0.53	0.00
FA-oleate	0.00	0.46	0.07

FA-oleate:TOPO	0.43	0.46	0.07
Cs-oleate	0.00	0.48	0.05
Cs-oleate:TOPO	0.43	0.48	0.05

Results

First, we examine the interaction of formamidinium oleate (FA-oleate) and cesium oleate (Cs-oleate), with OA and TOPO using proton (^{1}H) and phosphorous (^{31}P) NMR. The impact of (Cs, FA)-oleate on TOPO is investigated by examining ^{31}P NMR spectra. All NMR solutions are in d-toluene and their components and concentrations indicated in Table 1. In all cases, the (Cs, FA)-oleate solutions are in OA, so there is an excess of OA when either oleate precursor is present. We observe a downfield shift in the ^{31}P TOPO signal upon addition of OA, the extent of which is dictated by the concentration of OA (Figure S1), indicating a reduction in electron density shielding the probe nuclei, known as deshielding. In Figure 1a, we show that on replacement of neat OA with either 0.3 M Cs-oleate or 0.4 M FA-oleate in OA, there is a reduction in the extent of this shift. For Cs-oleate this is significant, with a difference of 1.63 ppm and is distinctly similar to a lower concentration of OA being present (Figure 1a, top panel). When FA-oleate is introduced, the difference in shift is less pronounced, clearly shown in Figure 1a (bottom panel), and only 0.43 ppm. This could indicate that less excess OA is interacting with the FA-oleate in comparison to Cs-oleate, or that there is a contribution from the FA-oleate that mimics the OA-TOPO interaction either from the amidinium ion or any residual acetic acid. In all cases, it is clear that the OA:TOPO interaction is influenced by the (Cs, FA)-oleate solution, albeit it to different extents.

To further probe the nature of the of influence of (Cs, FA)-oleate on the OA:TOPO interaction, we consider the acidic proton of OA. Due to the lability of acidic protons in solution, their NMR signal is downfield shifted (deshielded) and broad, and for neat OA in d-toluene such a peak at 12.2 ppm is observed (Figure S2). We observe in Figure 1b (top panel) that this proton signal in Cs-oleate in OA is shifted further downfield and considerably sharper. The opposite is true for FA-oleate in OA, which we show in Figure 1b (bottom panel), where we observe an upfield shift and broadening of the peak. The addition of TOPO to OA causes a downfield shift in the acidic proton (Figure S2), due to the acid-

base equilibrium, which has been investigated previously.[25] We observe the same impact for the (Cs, FA)-oleate solutions; in Figure 1b the arrows denote the shift from neat (Cs, FA)-oleate in OA (black line), to the (Cs, FA)-oleate:TOPO mixtures (blue or green line), which is larger for Cs-oleate than FA-oleate, at 0.15 ppm and 0.09 ppm respectively. The broadening of the peaks is clearer in normalised spectra, which we present in Figure S3.

Two conclusions can be drawn from this data. Firstly, FA and Cs have opposite effects on the acidic proton of OA, shown clearly in Figure 1b & S2. This is largely attributable to the introduction of labile protons on FA which are not present for Cs. Secondly, TOPO interacts with the acidic proton on OA in the same way for each sample (neat OA, Cs-oleate and FA-oleate). The extent or strength of this interaction may be influenced by the (Cs, FA)-oleate as seen by the extent of the peak shift and broadening.

Figure 1 a) ^{31}P NMR of Cs-oleate:TOPO, OA:TOPO (top) and FA-oleate:TOPO, OA:TOPO (bottom) at specified concentrations of OA. b) Normalised ^{1}H NMR spectra of acidic proton region of OA, with the top panel showing Cs-oleate, Cs-oleate:TOPO, OA:TOPO ([OA] = 0.48M) and OA ([OA] = 0.53 M) and the bottom panel showing FA-oleate, FA-oleate:TOPO, OA:TOPO ([OA] = 0.46 M) and OA ([OA] = 0.53 M). c) ^{1}H NMR spectra of methine proton region of FA for FA-oleate:TOPO (green, top) and FA-oleate (black, bottom). The broad peak marked with an asterisk (*) in the bottom panel is assigned to the labile amine protons. d) ^{1}H NMR spectra of methine proton region of FA for FA-oleate (black) and FA-oleate:TOPO (green) over temperature range 15 - 75 °C

We note that TOPO also induces a downfield shift in the methine proton of FA ($CH(NH_2)_2^+$). In Figure 1c the labile amine protons on FA ($CH(NH_2)_2^+$) are observable in neat FA-oleate as the broad peak centred around 8.3 ppm (marked with *, bottom panel), which is lost to baseline noise on the addition of TOPO (top panel). Given that the amine protons are observable without TOPO, it indicates that there is a possible interaction between these protons with TOPO, such as hydrogen bonding, resulting in a severe broadening of the peak.

Thus far, it is clear that the labile protons of FA cause a disruption in the OA:TOPO interaction, which is necessary for the formation of nanoparticles. In order to confirm the nature of this interaction, we undertook temperature dependent NMR experiments. We see in Figure 1d (left panel) that for FA-oleate in OA, the methine hydrogen undergoes only marginal changes over the temperature range of 15 to 75°C. When TOPO is present there is a significant upfield shift, Figure 1d (right panel). As the temperature is increased, the peak shifts back towards the position of the peak for neat FA-oleate.

Scheme 1 Representation of the euilibirum between OA:TOPO and FA-oleate:TOPO

As OA:TOPO are in an acid-base equilibrium,[25] higher temperatures correspond to more neutral TOPO being present. We propose that FA and TOPO are in a similar equilibrium, and that the methine shifts correlate to a release of FA from TOPO at higher temperatures, while the equilibrium is pushed towards the neutral forms of FA and TOPO. The temperature effects on the acidic proton of OA and the phosphorus in TOPO are shown in Figure S4 where the change in the shift and width of the peaks corroborate the existence of an interaction equilibrium between FA and TOPO.[25,28] We include further discussion of these results in the Supporting Information.

From this data, we can establish that there are two competing interactions in the FA-oleate:TOPO solutions. There is an equilibrium between the FA-oleate:TOPO alongside the equilibrium of OA:TOPO, as compared to them being free in solution. The coexistence of these two interactions leads to an overall exchange of OA:TOPO with FA-oleate:TOPO, which we depict in Scheme 1, and we have alluded to the nature of these interactions further in the Supporting Information, Figure S5.

Nanocrystal Synthesis We now proceed to examine the synthesis of $FAPbBr_3$ nanoparticles, with consideration of the NMR results that we have discussed above. For the standard synthesis we dissolve lead bromide in TOPO and OA in ODE at 75 °C and then set the reaction mixture to the desired temperature (23 °C to 75 °C). We inject FA-oleate (in OA) and after 30 seconds, we quench the reaction in an ice bath. The nanoparticles are separated by centrifugation at 5,000 rpm for 10 minutes, and the crude product consisting of a solid pellet, and an oily residue is redispersed in hexane. From ICP-OES,

we determine that the yield of lead bromide converted to perovskite is 15.3 atom % in lead. We depict the process in Figure 2a, and present comprehensive experimental details in the Experimental section at the end of this manuscript.

Figure 2 a) Scheme of phosphine oxide injection route to $FAPbBr_3$ nanoparticles and b) PL (black dash) and absorption (green solid) spectra for nanoparticles made at 23, 55 and 75 °C

We performed the synthesis at temperatures ranging from room temperature (19-23 °C) to 75 °C. These temperatures are significantly lower than previous reports of $FAPbBr_3$ nanocrystals synthesised by the hot-injection method, which were conducted between 80 and 130 °C.[11] We show in Figure 2b the blue shift in photoluminescence (PL) peak with decreasing reaction temperature, from 2.31 eV to 2.40 eV. This is a small shift in PL peak for a 50 °C range with only a 0.10 eV difference in peak maxima from 75 to 23 °C. In contrast, the hot-injection synthesis of $FAPbBr_3$ results in a 0.35 eV shift for a 50 °C range (80 - 130 °C).[11] Here, we also observe an increase in full-width at half-maximum (FWHM) and photoluminescence quantum yield (PLQY) with decreasing temperature, and measure PLQE values of approximately 70 % in solution, for the room temperature synthesis (Figure S6). For the room temperature growth, we observe a negligible effect on the optical properties of the nanoparticles with reaction time, as we show in Figure S7. This is most likely due to a lack of ripening and size defocusing over time, in a similar way to that of $CsPbBr_3$ made through the TOPO route.[25]

We investigate the effect of OA:TOPO molar ratio on the $FAPbBr_3$ nanoparticle synthesis by varying both the OA and TOPO content. In all cases, the OA concentration is the sum of the OA in the lead halide solution and in the injection of the FA-oleate in OA. We carried out the reactions at three temperatures: room temperature (19-23 °C), 40 °C and 55 °C.

We show the PL peak, FWHM, and the PLQY in Figure 3a-c, and observe a distinct decrease in peak energy, or red shift, in the PL emission for an increasing ratio of OA:TOPO. We also observe reduction

of the FWHM as the OA:TOPO ratio is increased from 0.8:1 to 2:1. The PLQY increases with an increasing OA:TOPO ratio, but in this case, it also goes through a maximum. The shaded region of Figure 3c, between 1.2:1 and 1.6:1 OA:TOPO, is where we determine the highest PLQY values for each temperature. Outside of this shaded region, the PLQY is significantly lower and increasing the temperature also induces a further decrease, dropping from 70 % at room temperature to 30 % at 55 °C.

Figure 3 Optical properties of $FAPbBr_3$ nanoparticles synthesised at room temperature (rT, black), 40 (green), and 55 °C (red) with varying molar ratio of OA:TOPO. a) PL peak position, b) FWHM, c) PLQY, with the regions of interest highlighted by the grey box, and d) absorption spectra (solid line) with associated PL overlaid (dashed line)

The OA:TOPO ratio can be finely tuned by changing the concentration of FA-oleate in the injection solution. Varying the FA-oleate concentration between 0.1 and 0.4 M, tunes the OA:TOPO ratio between 1.68:1 and 1.56:1. We see the effect of this tuning in Figure S8, with a general blue shift in PL peak alongside an increase in FWHM and PLQY. The concentration of FA could have an influence on the nanoparticles but decoupling this from the larger influence of the OA:TOPO ratio is complex, and thus we evaluate it as part of the OA:TOPO ratio instead. The PL is similarly impacted by temperature, where we observe more extreme changes in the PL peak position, FWHM and PLQY at room temperature, as compared to 55 °C. For $CsPbBr_3$ nanocubes, the concentration of Cs-oleate could be directly correlated to the ligand coverage since it only influenced the PLQY as opposed to the peak position and FWHM.[25] The changes in PL peak and FWHM observed here for $FAPbBr_3$ nanoparticles, alongside the NMR data discussed previously, indicate that there is a more complex picture for the $FAPbBr_3$ system. Similarly, due to the small change in OA:TOPO ratio coupled with the

impact on optical properties, it is clear that the FA-oleate:TOPO interaction is interfering with the metathesis reaction of $PbBr_2$ and FA.

In Figure 3d we present the absorption spectra of nanoparticles made at varying OA:TOPO ratios and temperature. Features in the absorption spectra above 2.75 eV are observed, and as the OA:TOPO ratio decreases these peaks are more prominent and we lose the sharp absorption onset, which is amplified at lower reaction temperatures. We assume these features in the UV-Vis absorption spectra arise from a certain fraction of lower dimensional phases being present but discuss the potential origin in more detail in the Supporting Information. Despite a shallow absorption onset at 2.3 eV for the low temperature and low ratio samples, the PL profile is similar for all samples.

Figure 4 TEM of $FAPbBr_3$ nanoparticles synthesised at varying ratios of OA: TOPO, with reaction temperatures of a) room temperature (rT) and b) 55 °C. c) XRD of $FAPbBr_3$ nanoparticles synthesised at room temperature (rT) with varying molar ratio of OA:TOPO. The XRD is measured under air-free conditions using a dome holder, with reference pattern for the dome shown in green and a simulated XRD pattern for $FAPbBr_3$ shown in red

We observe a change in the shape of the nanocrystals, with a deviation from nanocubes, as shown in the TEM images presented in Figure 4a & b. $FAPbBr_3$ nanoparticles synthesised at room temperature are large, rounded particles, with a lack of shape homogeneity at low OA:TOPO ratios. More cubic or rectangular particles are formed at an OA:TOPO ratio of 1.56:1, but there is little uniformity across the sample. At 55 °C, smaller particles are formed that are more spherical in shape, and an increase in ratio from 1.19:1 to 1.81:1 does not yield distinct differences.

An explanation for the unusual optical and structural properties of our $FAPbBr_3$ nanocrystals, is the intercalation of TOPO between layers of $FAPbBr_3$. Since previous studies have shown that dimethyl sulfoxide (DMSO) can intercalate into polycrystalline $FAPbBr_3$[29], and that there are similarities in the binding groups of TOPO and DMSO, the mechanism for intercalation here is plausible.

However, the XRD of the crude solid pellet presented in Figure 4c suggests that a 3D perovskite structure has formed; the peaks match a simulated pattern for 3D cubic $FAPbBr_3$. In all cases, the XRD signal is very weak and there is a clear decrease in intensity with an increasing OA:TOPO ratio. No shifts or additional peaks appear with the changing ratio, as would be expected with the presence of TOPO intercalation, and the corresponding absorption data for these samples do not display any features above 2.5 eV (Figure S9). See Supporting Information for further discussion.

On balance, the data presented suggests that the crude nanoparticles, consisting of a solid pellet and oily residue, need to be purified. Furthermore, by introducing an anti-solvent into the initial separation step, followed by additional washing steps, there is also the opportunity to alleviate the polydispersity and shape irregularity of the particles.

The influence of Washing $FAPbBr_3$ nanoparticles were synthesised at room temperature with a OA:TOPO ratio of 1.56:1, and were subsequently precipitated with acetonitrile and toluene, affording the samples **Sep** (separated from reaction mixture), **Wash** (separated and then washed), and **Wash + OA** (separated, OA added, and then washed). Full details of washing procedures can be found in the Experimental section. Films of these nanoparticles were made by drop casting from hexane:octane (9:1) and left to dry without annealing.

As expected, in Figure 5a we observe no features in the absorption spectra above 2.75 eV with the chosen OA:TOPO ratio of 1.56:1, and additional separation and washing steps induce a steepening of the absorption onset. When the nanoparticle solutions are coated into films, we observe small differences in the PL spectra. In solution, washing the nanoparticles induces a red shift and narrowing of the PL peak which is further enhanced with the addition of OA. This is consistent with a reduction of size distribution after washing, with the red shift indicating that the nanoparticles are on average larger, either as small particles are removed or merged with larger ones. However, in the films there is little difference in the FWHM across all three samples, and only the addition of OA causes the PL of the film to be red shifted (Figure 5a and S9).

We find that the PLQY of the nanoparticle solution suffers greatly through the separation and washing steps, where we observe a drop of 30 % absolute, which we show in Figure 5b. Previously, the addition of OA maintained a high PLQY for $CsPbBr_3$ nanocrystals,[25] whereas we see here that it causes a decrease in the PLQY. However, when deposited as films there is very little difference in the PLQY between different samples. Surprisingly, a solution with a PLQY lower than 20 % can still yield a film with approximately 50 % PLQY. This may be a result of the merging of the nanoparticles during film formation, with a consistent FWHM suggesting an averaging of the sizes of particles present (Figure S10), whilst also improving the ligand surface coverage. This is encouraging behaviour for LED device applications, since when washed there are fewer ligands around to disrupt the charge transfer, but a high PLQY is maintained.

Figure 5 Optical properties of $FAPbBr_3$ nanoparticles washed in three different ways in solution (Sep, Wash, Wash + OA). a) PL and absorption spectra and b) PLQY of solutions and drop cast films on glass. c) champion external quantum efficiency (EQE) of LED made from washed $FAPbBr_3$ nanoparticles and d) the electroluminescence of the device, centred at 2.32 eV with a FWHM of 90 meV

We conducted TEM imaging to assess if the washing processes affects the structure of the nanoparticles and the micrographs are presented in Figure S13. When the nanoparticles are washed, they have a more defined hexagonal shape as opposed to rounded, as seen in Figure 4 & b. As seen above, the optical properties of the $FAPbBr_3$ nanoparticles appear to converge when made into a film. This questions whether what is seen in the TEM for these materials is a true reflection of what is in the solution. Regardless, there is no dramatic difference in the TEM when the nanoparticles are washed or not, and no nanocubes are observed.

In order to assess the functionality of these nanoparticles in an optoelectronic devices, we fabricated light emitting diodes (LEDs) using the architecture of indium-doped tin oxide (ITO)/Poly(4-butylphenyldiphenylamine) (Poly-TPD)/$FAPbBr_3$/ 2,2',2"-(1,3,5-Benzinetriyl)-tris(1-phenyl-1-H-benzimidazole) (TPBi)/Lithium fluoride (LiF)/Aluminium (Al). $FAPbBr_3$ nanoparticles were spin-coated from octane in a glovebox, and the devices were measured in a nitrogen-filled sample holder.

We compare the champion EQE of each device set in Figure S11 and, as expected, the most efficient device has the least amount of ligand, named "sample **Wash**". When not enough ligands are washed away (**Sep**) then the device does not turn on, and where additional OA is added (**Wash + OA**) the device performance is low, likely due to an excess of long ligands in the film impeding charge injection or transport. Through device stack optimisation, we are able to obtain LEDs with a maximum EQE of 3.7 % at 2.32 eV (534 nm), presented in Figure 5c & d, which are in line with the state of the art for $FAPbBr_3$ colloidal nanoparticle based LEDs.[30–33] Further device characterisation and device statistics can be found in Figure S12. Given the high PLQY of the nanoparticle films, the device properties reported are far from the limit that this route has to offer. We expect that with further refinement of the device stack, balancing of charges, and ligand manipulation that significant improvements in LEDs with these nanoparticles will be achieved.

Discussion From our understanding we can develop a schematic representation of the reaction pathway for the synthesis of $FAPbBr_3$ nanocrystal via the TOPO route, which we depict in Scheme 2. From the work of Almeida et al, we learn that the TOPO:$PbBr_2$ complex is disrupted by the addition of OA in the Cs-oleate injection step,[25] and this is represented in reaction 1. In this work, we have shown the existence of another equilibrium (2), where the FA-oleate:TOPO is competing with the OA:TOPO complex. The mediation of this equilibrium to release FA-oleate, is required for the formation of $FAPbBr_3$ nanoparticles through reaction with lead bromide, reaction 3.

This interaction (2) has two main impacts on the synthesis of $FAPbBr_3$ nanoparticles. Firstly, the proportion of FA available to readily react with the lead halide to form the perovskite will be impeded.

The phosphine oxide synthesis gave record yields for $CsPbBr_3$ nanocrystals, but this is not replicated here with only 15.3 atom % in Pb yielded of the crude product, determined by ICP-OES. Secondly, the ligand coverage on the surface of the nanoparticles will be impacted, and the interaction may promote TOPO to be on the surface of $FAPbBr_3$. Having such a large molecule on the surface could easily disrupt ligand packing and the shape of the nanoparticles, which can explain the absence of nanocubes.

In Scheme 2 we depict oleate-only capping of the nanoparticles, but the optical and structural data for the washed $FAPbBr_3$ nanoparticles support the hypothesis of a more complex ligand shell being present. Adding back OA would have increased the PLQY of oleate-only capped nanoparticles through manipulation of the ligand equilibrium between the surface and solution, as seen for $CsPbBr_3$ nanocrystals[25]. Since the addition of OA in the washing steps induces a further decrease in PLQY instead, there is a disruption in the surface coverage of the ligand shell. This is potentially due to OA interacting with any TOPO on the surface of the nanoparticles in a competing pathway. This would draw TOPO away from the surface, leaving dangling bonds to act as trap-states for charge carriers and quenching the PLQY. For future improvement of LED devices, optimizing a ligand exchange would be an important step to maintain the high PLQY of the nanoparticles and improve the charge transport capabilities.

Scheme 2 Representation of the reaction pathway for the phosphine oxide route to $FAPbBr_3$ nanoparticles

We have shown that the OA:TOPO ratio plays a pivotal role in the optical and structural properties of $FAPbBr_3$ nanoparticles. Ratios between 1.2 and 1.6 result in higher PLQYs and less pronounced features above 2.75 eV in the absorption spectra. At higher amounts of OA there is less neutral TOPO available to interact with FA, due to the OA:TOPO interaction dominating. Conversely, lower temperatures enhance these properties further, with a PLQY up to 70 %, which is the highest reported so far for a room temperature synthesis of $FAPbBr_3$. Since we have shown that FA and TOPO engage in an equilibrium, lower temperatures will promote their interaction. Therefore, it would appear that

the FA-oleate:TOPO interaction is not wholly detrimental to the formation of $FAPbBr_3$ nanoparticles of some form. This relationship must be balanced in order to form highly luminescent material.

In comparisons to nanoparticles synthesized via the standard Hot Injection or LARP syntheses,[11,12,23,24] our route is less energy intensive, with reactions conducted at low temperatures and in air. However, the tunability of the band gap via size control, and narrow FWHM of the PL spectra are lacking in the colloidal nanoparticles formed by our new synthetic route. Nevertheless, when processed into a solid thin-film, we obtain very high PLQYs, with a narrow PL FWHM of 90 meV (< 25 nm), and at an industrially ideal wavelength from green emission in displays. Importantly, our nanoparticles perform comparably well as compared with LARP synthesised nanaoparticles, when incorporated into LEDs.[30–33]

Conclusion

In this work, we have demonstrated that the labile amine protons on FA are engaged in an equilibrium with TOPO, which consequently impedes the metathesis reaction of $PbBr_2$ and FA. This shows the need to control any basic molecule in a synthesis with FA, not just ammonium based molecules such as OLAm. As a result, the phosphine oxide synthesis of $FAPbBr_3$ does not result in the desired monodisperse nanocubes, as obtained for $CsPbBr_3$. Despite this, we have shown that this synthesis of $FAPbBr_3$ nanoparticles can be conducted at room temperature, and we have presented solutions with 70% PLQY, films with PLQY of over 50% and LED devices with over 3% EL-EQE, operating at the desired green-channel wavelength of 2.34 eV (530 nm).

Overall, we have demonstrated highly luminescent $FAPbBr_3$ nanoparticles formed through a phosphine oxide synthesis at room temperature, which is free from rapid size defocusing or ripening. The time independence and low temperature make this synthesis a potential for continuous flow processes, which are more feasibly scalable.

Experimental

Materials All chemicals were used as purchased without further purification. 1-octadecene (ODE, 90 %, Sigma Aldrich), 2,2',2"-(1,3,5-Benzinetriyl)-tris(1-phenyl-1-H-benzimidazole) (TPBi, Ossila), acetonitrile (99.8 %, Sigma Aldrich), cesium carbonate (Cs_2CO_3, 99.9 %, Sigma Aldrich), chlorobenzene (99.8 % , Sigma Aldrich), formamidinium acetate salt (99 %, Sigma Aldrich), lead bromide ($PbBr_2$, >98 % , Sigma Aldrich), lithium fluoride (LiF, >99.99 %, Lumtec**)**, n-hexane (95 %, Sigma Aldrich), octane (>99 %, Sigma Aldrich), oleic acid (OA, 90 %, Sigma Aldrich), poly[N,N'-bis(4-butylphenyl)-N,N'-bisphenylbenzidine] (Poly-TPD, Ossila) toluene (99.8 %, Sigma Aldrich) and trioctylphosphine oxide (TOPO, 99%, Sigma Aldrich).

0.3 M Cs-oleate in OA Cs_2CO_3 (0.244 g, 0.76 mmol) and OA (5.0 mL, 15.8 mmol) are degassed in a 3-neck round-bottomed flask under vacuum at 100 °C for 1 hour followed by reacting under nitrogen at 140 °C. The colourless Cs-oleate solution is stored in a nitrogen filled vial for further use.

0.4 M FA-oleate in OA OA (40 mL) is dried at 120 °C for 1 hour. Formamidinium acetate (1.66 g, 15.9 mmol) is added and the mixture is degassed at 50 °C for 15 minutes. The temperature is raised to 130 °C under nitrogen until all the formamidinium acetate has dissolved. The FA-oleate solution is then cooled and stored under nitrogen until further use.

$FAPbBr_3$ Nanocrystals The synthetic procedures are carried out in air, unless otherwise stated. All reactions are performed in vials on a hot plate equipped with a thermocouple and a magnetic stirrer at 800 rpm. In a typical synthesis, $PbBr_2$ (60 mg, 0.16 mmol), TOPO (1.0 g, 0.88 g/mL, 2.59 mmol) and OA (400 µL, 1.27 mmol) are heated to 75 °C in ODE (5.0 mL), providing a clear solution. The temperature is set to the desired reaction temperature (between room temperature and 75 °C) and FA-oleate is injected (0.4 M, 1.0 mL), which has been pre-heated to the desired temperature. Depending on the chosen temperature, the injection of FA-oleate immediately turns the initially colourless Pb-solution green or yellow, indicating the formation of $FAPbBr_3$. After 30 seconds of growth, the vial is plunged into an ice bath to quench the reaction. In the absence of an anti-solvent the nanocrystals are separated by centrifugation at 5,000 rpm for 10 minutes and redispersed in hexane.

Washing

Sep The nanoparticles are separated from the reaction mixture by adding an equal volume of toluene and half volume of acetonitrile with respect to the reaction mixture volume. The nanoparticles are then centrifuged at 5,000 rpm for 10 minutes. The supernatant is discarded, and the nanoparticles are redispersed in octane or a hexane:octane mix. Using this procedure, no oily residue is obtained – only a solid pellet of nanocrystals.

Wash The nanoparticles are separated from the solution as before, using toluene and acetonitrile. The nanoparticles are redispersed in toluene, and acetonitrile is added at a 2:1 volume ratio. The mixture is then centrifuged at 3,000 rpm for 5 minutes. The supernatant is discarded, and the nanoparticles are redispersed in octane or a hexane:octane mix.

Wash + OA The nanoparticles are washed as for the previous case, but upon redispersal in toluene after the initial separation, a small amount of oleic acid is added back to the nanoparticles. Acetonitrile is then added before centrifuging and redispersing again.

Film Fabrication Films for characterisation are made from nanocrystal solutions drop cast from concentrated solutions in a mixed solvent system: hexane and octane in a 9:1 ratio.

Device Fabrication ITO/Poly-TPD/$FAPbBr_3$/TPBi/LiF/Al ITO substrates are cleaned with acetone and isopropanol prior to device fabrication. 50 µL of a 10 mg/mL Poly[N,N’-bis(4-butylphenyl)-N,N’-bisphenylbenzidine] (Poly-TPD) solution in chlorobenzene is spincoated at 4000 rpm for 30 seconds, followed by a 10 minute anneal at 130 °C. Then, $FAPbBr_3$ nanoparticles which have been washed (either Sep, Wash, or Wash + OA) and have been redispersed in 2.4 mL octane and 75 µL of this solution are dynamically spin coated under inert atmosphere, at 750 rpm for 30 seconds followed by 6000 rpm for 10 seconds. The samples are then moved to a glovebox evaporator where 50 nm of 2,2',2"-(1,3,5-Benzinetriyl)-tris(1-phenyl-1-H-benzimidazole) (TPBi) is evaporated, followed by a 3 nm layer of lithium floride (LiF) and aluminium (Al) electrodes. Devices are further modified by introducing a 2 nm thick layer of LiF on top of the poly-TPD before the $FAPbBr_3$ nanoparticles are spun on top.

Optical Characterisation Measurements are either recorded on colloidal solutions or on thin films. Measurements in solution have been carried out in 1 cm quartz cuvettes. Steady-State Photoluminescence (PL) Spectroscopy is conducted on a Horiba Scientific Fluorolog. Ultraviolet-Visible Absorption Spectroscopy (UV-vis) is conducted on an Agilent Technologies Cary 60 UV Vis. Photoluminescence Quantum Yield (PLQY) is measured with a CNI Low Noise Violet Blue 405 nm 200 mW laser with an integrating sphere and Ocean Optics Maya2000 Pro spectrometer. The integrating sphere allows for redistribution of light isotropically, regardless of angular dependence of emission. The system, including the sphere, fibre and spectrometer, was calibrated using a calibration halogen lamp. The PLQY is calculated according to De Mello et al, taking reabsorption into account.[34]

X-ray diffraction (XRD) The pellet of the crude nanoparticle product is smeared onto a quartz disc in a nitrogen filled glovebox. The samples are loaded into air-free XRD holders with a dome (green trace, Figure 4) over the top of the sample to maintain an inert atmosphere during measurement. PANalytical X'Pert Pro powder diffractometer is used, with a Cu-Kα radiation operating at 40 kV and 40 mA.

Transmission Electron Microscopy (TEM) A Jeol JEM-2100 microscope with LaB_6 source, operating at an accelerating voltage of 200 kV is used. It has a Gatan Orius CCD camera. TEM is carried out in the David Cockayne Centre for Electron Microscopy, Department of Materials, University of Oxford. Nanocrystal dispersions are drop cast onto holey-carbon coated 300 mesh copper grids.

Nuclear Magnetic Resonance Spectroscopy (NMR) A 2-channel Bruker Avance III HD 400 MHz nanobay instrument running TOPSPIN 3 equipped with a 5 mm z-gradient Broad Band Fluorine Observation probe is used. For ^{1}H NMR residual d-toluene peaks are used for reference. For ^{31}P NMR, an external standard of triethylphosphate is used. The temperature dependents measurements on FA-oleate and FA-oleate:TOPO were conducted on a four-channel Bruker AVIII HD 500 running TOPSPIN 3 equipped with a SampleCase 24 sample robot and a 5 mm triple-resonance TBO probe with multinuclear capability and a BCU-II temperature regulation unit. Spectra were taken at 10 °C intervals from 15 to 75 °C.

ASSOCIATED CONTENT

Supporting Information. The following files is available free of charge. Additional NMR, synthetic optimization, and device characterization data can be found in the Supporting Information PDF.

AUTHOR INFORMATION

Corresponding Author

*Bernard Wenger: bernard.wenger@physics.ox.ac.uk

*Henry J. Snaith: henry.snaith@physics.ox.ac.uk

Author Contributions

The manuscript was written through contributions of all authors. All authors have given approval to the final version of the manuscript.

Funding Sources

This work was part funded by the Engineering and Physical Science Research Council (EPSRC), UK, on grant EP/P032591/1 and EP/L01551X/1. OJA extends thanks to their additional funding sources at Oxford PV Ltd and the Radcliffe Scholarship from University College, Oxford.

ACKNOWLEDGMENT

The authors extend thanks to Dr Nader Amin (Department of Chemistry, University of Oxford, UK) for the temperature dependent NMR measurements and Filipo Drago for the ICP-OES measurements (Nanochemistry Department, Instituto Italiano Tecnologia, Italy). For helpful discussions the authors thank Dr Liberato Manna (Nanochemistry Department, Instituto Italiano Tecnologia, Italy).

References

(1) Pan, J.; Quan, L. N.; Zhao, Y.; Peng, W.; Murali, B.; Sarmah, S. P.; Yuan, M.; Sinatra, L.; Alyami, N. M.; Liu, J.; Yassitepe, E.; Yang, Z.; Voznyy, O.; Comin, R.; Hedhili, M. N.; Mohammed, O. F.;

Lu, Z. H.; Kim, D. H.; Sargent, E. H.; Bakr, O. M. Highly Efficient Perovskite-Quantum-Dot Light-Emitting Diodes by Surface Engineering. *Adv. Mater.* **2016**, *28* (39), 8718–8725. https://doi.org/10.1002/adma.201600784.

(2) Levchuk, I.; Herre, P.; Brandl, M.; Osvet, A.; Hock, R.; Peukert, W.; Schweizer, P.; Spiecker, E.; Batentschuk, M.; Brabec, C. J. Ligand-Assisted Thickness Tailoring of Highly Luminescent Colloidal $CH_3NH_3PbX_3$ (X = Br and I) Perovskite Nanoplatelets. *Chem. Commun.* **2017**, *53* (1), 244–247. https://doi.org/10.1039/C6CC09266G.

(3) Weidman, M. C.; Seitz, M.; Stranks, S. D.; Tisdale, W. A. Highly Tunable Colloidal Perovskite Nanoplatelets through Variable Cation, Metal, and Halide Composition. *ACS Nano* **2016**, *10* (8), 7830–7839. https://doi.org/10.1021/acsnano.6b03496.

(4) Levchuk, I.; Osvet, A.; Tang, X.; Brandl, M.; Perea, J. D.; Hoegl, F.; Matt, G. J.; Hock, R.; Batentschuk, M.; Brabec, C. J. Brightly Luminescent and Color-Tunable Formamidinium Lead Halide Perovskite $FAPbX_3$ (X = Cl, Br, I) Colloidal Nanocrystals. *Nano Lett.* **2017**, *17* (5), 2765–2770. https://doi.org/10.1021/acs.nanolett.6b04781.

(5) Minh, D. N.; Kim, J.; Hyon, J.; Sim, J. H.; Sowlih, H. H.; Seo, C.; Nam, J.; Eom, S.; Suk, S.; Lee, S.; Kim, E.; Kang, Y. Room-Temperature Synthesis of Widely Tunable Formamidinium Lead Halide Perovskite Nanocrystals. *Chem. Mater.* **2017**, *29* (13), 5713–5719. https://doi.org/10.1021/acs.chemmater.7b01705.

(6) Li, X.; Wu, Y.; Zhang, S.; Cai, B.; Gu, Y.; Song, J.; Zeng, H. CsPbX$_{3}$ Quantum Dots for Lighting and Displays: Room-Temperature Synthesis, Photoluminescence Superiorities, Underlying Origins and White Light-Emitting Diodes. *Adv. Funct. Mater.* **2016**, *26* (15), 2435–2445. https://doi.org/10.1002/adfm.201600109.

(7) Seth, S.; Samanta, A. A Facile Methodology for Engineering the Morphology of $CsPbX_3$ Perovskite Nanocrystals under Ambient Condition. *Sci. Rep.* **2016**, *6* (1), 37693.

https://doi.org/10.1038/srep37693.

(8) Shamsi, J.; Rastogi, P.; Caligiuri, V.; Abdelhady, A. L.; Spirito, D.; Manna, L.; Krahne, R. Bright-Emitting Perovskite Films by Large-Scale Synthesis and Photoinduced Solid-State Transformation of $CsPbBr_3$ Nanoplatelets. *ACS Nano* **2017**, *11* (10), 10206–10213. https://doi.org/10.1021/acsnano.7b04761.

(9) Wei, S.; Yang, Y.; Kang, X.; Wang, L.; Huang, L.; Pan, D. Room-Temperature and Gram-Scale Synthesis of $CsPbX_3$ (X = Cl, Br, I) Perovskite Nanocrystals with 50–85 % Photoluminescence Quantum Yields. *Chem. Commun.* **2016**, *52* (45), 7265–7268. https://doi.org/10.1039/C6CC01500J.

(10) Protesescu, L.; Yakunin, S.; Bodnarchuk, M. I.; Krieg, F.; Caputo, R.; Hendon, C. H.; Yang, R. X.; Walsh, A.; Kovalenko, M. V. Nanocrystals of Cesium Lead Halide Perovskites ($CsPbX_3$, X = Cl, Br, and I): Novel Optoelectronic Materials Showing Bright Emission with Wide Color Gamut. *Nano Lett.* **2015**, *15* (6), 3692–3696. https://doi.org/10.1021/nl5048779.

(11) Protesescu, L.; Yakunin, S.; Bodnarchuk, M. I.; Bertolotti, F.; Masciocchi, N.; Guagliardi, A.; Kovalenko, M. V. Monodisperse Formamidinium Lead Bromide Nanocrystals with Bright and Stable Green Photoluminescence. *J. Am. Chem. Soc.* **2016**, No. Figure 1, jacs.6b08900. https://doi.org/10.1021/jacs.6b08900.

(12) Protesescu, L.; Yakunin, S.; Kumar, S.; Bär, J.; Bertolotti, F.; Masciocchi, N.; Guagliardi, A.; Grotevent, M.; Shorubalko, I.; Bodnarchuk, M. I.; Shih, C.-J.; Kovalenko, M. V. Dismantling the "Red Wall" of Colloidal Perovskites: Highly Luminescent Formamidinium and Formamidinium–Cesium Lead Iodide Nanocrystals. *ACS Nano* **2017**, *11* (3), 3119–3134. https://doi.org/10.1021/acsnano.7b00116.

(13) Wang, A.; Guo, Y.; Muhammad, F.; Deng, Z. Controlled Synthesis of Lead-Free Cesium Tin Halide Perovskite Cubic Nanocages with High Stability. *Chem. Mater.* **2017**, *29* (15), 6493–

6501. https://doi.org/10.1021/acs.chemmater.7b02089.

(14) Vybornyi, O.; Yakunin, S.; Kovalenko, M. Polar-Solvent-Free Colloidal Synthesis of Highly Luminescent Alkylammonium Lead Halide Perovskite Nanocrystals. *Nanoscale* **2015**, 2–7. https://doi.org/10.1039/C5NR06890H.

(15) Shamsi, J.; Urban, A. S.; Imran, M.; De Trizio, L.; Manna, L. Metal Halide Perovskite Nanocrystals: Synthesis, Post-Synthesis Modifications, and Their Optical Properties. *Chem. Rev.* **2019**, *119* (5), 3296–3348. https://doi.org/10.1021/acs.chemrev.8b00644.

(16) De Roo, J.; Ibáñez, M.; Geiregat, P.; Nedelcu, G.; Walravens, W.; Maes, J.; Martins, J. C.; Van Driessche, I.; Kovalenko, M. V.; Hens, Z. Highly Dynamic Ligand Binding and Light Absorption Coefficient of Cesium Lead Bromide Perovskite Nanocrystals. *ACS Nano* **2016**, *10* (2), 2071–2081. https://doi.org/10.1021/acsnano.5b06295.

(17) Chang, J.; Waclawik, E. R. Colloidal Semiconductor Nanocrystals: Controlled Synthesis and Surface Chemistry in Organic Media. *RSC Adv.* **2014**, *4* (45), 23505–23527. https://doi.org/10.1039/c4ra02684e.

(18) Yin, Y.; Alivisatos, A. P. Colloidal Nanocrystal Synthesis and the Organic–inorganic Interface. *Nature* **2005**, *437* (7059), 664–670. https://doi.org/10.1038/nature04165.

(19) Carey, G. H.; Abdelhady, A. L.; Ning, Z.; Thon, S. M.; Bakr, O. M.; Sargent, E. H. Colloidal Quantum Dot Solar Cells. *Chem. Rev.* **2015**, *115* (23), 12732–12763. https://doi.org/10.1021/acs.chemrev.5b00063.

(20) LaMer, V. K.; Dinegar, R. H. Theory, Production and Mechanism of Formation of Monodispersed Hydrosols. *J. Am. Chem. Soc.* **1950**, *72* (11), 4847–4854. https://doi.org/10.1021/ja01167a001.

(21) Thanh, N. T. K.; Maclean, N.; Mahiddine, S. Mechanisms of Nucleation and Growth of

Nanoparticles in Solution. *Chem. Rev.* **2014**, *114* (15), 7610–7630. https://doi.org/10.1021/cr400544s.

(22) Krieg, F.; Ochsenbein, S. T.; Yakunin, S.; ten Brinck, S.; Aellen, P.; Süess, A.; Clerc, B.; Guggisberg, D.; Nazarenko, O.; Shynkarenko, Y.; Kumar, S.; Shih, C.-J.; Infante, I.; Kovalenko, M. V. Colloidal $CsPbX_3$ (X = Cl, Br, I) Nanocrystals 2.0: Zwitterionic Capping Ligands for Improved Durability and Stability. *ACS Energy Lett.* **2018**, *3* (3), 641–646. https://doi.org/10.1021/acsenergylett.8b00035.

(23) Perumal, A.; Shendre, S.; Li, M.; Tay, Y. K. E.; Sharma, V. K.; Chen, S.; Wei, Z.; Liu, Q.; Gao, Y.; Buenconsejo, P. J. S.; Tan, S. T.; Gan, C. L.; Xiong, Q.; Sum, T. C.; Demir, H. V. High Brightness Formamidinium Lead Bromide Perovskite Nanocrystal Light Emitting Devices. *Sci. Rep.* **2016**, *6* (1), 36733. https://doi.org/10.1038/srep36733.

(24) Tong, Y.-L.; Zhang, Y.-W.; Ma, K.; Cheng, R.; Wang, F.; Chen, S. One-Step Synthesis of FA-Directing $FAPbBr_3$ Perovskite Nanocrystals toward High-Performance Display. *ACS Appl. Mater. \& Interfaces* **2018**, *10* (37), 31603–31609. https://doi.org/10.1021/acsami.8b10366.

(25) Almeida, G.; Ashton, O. J.; Goldoni, L.; Maggioni, D.; Petralanda, U.; Mishra, N.; Akkerman, Q. A.; Infante, I.; Snaith, H. J.; Manna, L. The Phosphine Oxide Route toward Lead Halide Perovskite Nanocrystals. *J. Am. Chem. Soc.* **2018**, *140* (44), 14878–14886. https://doi.org/10.1021/jacs.8b08978.

(26) De Roo, J.; De Keukeleere, K.; Hens, Z.; Van Driessche, I. From Ligands to Binding Motifs and Beyond; The Enhanced Versatility of Nanocrystal Surfaces. *Dalt. Trans.* **2016**, *45* (34), 13277–13283. https://doi.org/10.1039/c6dt02410f.

(27) Almeida, G.; Goldoni, L.; Akkerman, Q.; Dang, Z.; Khan, A. H.; Marras, S.; Moreels, I.; Manna, L. Role of Acid–Base Equilibria in the Size, Shape, and Phase Control of Cesium Lead Bromide Nanocrystals. *ACS Nano* **2018**, *12* (2), 1704–1711. https://doi.org/10.1021/acsnano.7b08357.

(28) Maciel, G. E.; James, R. V. Solvent Effects on the Phosphorus-31 Chemical Shift in Triphenylphosphine Oxide. *Inorg. Chem.* **1964**, *3* (11), 1650–1651. https://doi.org/10.1021/ic50021a046.

(29) Shin, M.; Kim, J.; Jung, Y.-K.; Ruoko, T.; Priimagi, A.; Walsh, A.; Shin, B. Low-Dimensional Formamidinium Lead Perovskite Architectures via Controllable Solvent Intercalation. *J. Mater. Chem. C* **2019**, *7* (13), 3945–3951. https://doi.org/10.1039/C9TC00379G.

(30) Li, Y.-F.; Feng, J.; Sun, H.-B. Perovskite Quantum Dots for Light-Emitting Devices. *Nanoscale* **2019**, *11* (41), 19119–19139. https://doi.org/10.1039/C9NR06191F.

(31) Kim, Y.-H.; Lee, G.-H.; Kim, Y.-T.; Wolf, C.; Yun, H. J.; Kwon, W.; Park, C. G.; Lee, T.-W. High Efficiency Perovskite Light-Emitting Diodes of Ligand-Engineered Colloidal Formamidinium Lead Bromide Nanoparticles. *Nano Energy* **2017**, *38*, 51–58. https://doi.org/10.1016/j.nanoen.2017.05.002.

(32) Fang, H.; Deng, W.; Zhang, X.; Xu, X.; Zhang, M.; Jie, J.; Zhang, X. Few-Layer Formamidinium Lead Bromide Nanoplatelets for Ultrapure-Green and High-Efficiency Light-Emitting Diodes. *Nano Res.* **2019**, *12* (1), 171–176. https://doi.org/10.1007/s12274-018-2197-3.

(33) Han, D.; Imran, M.; Zhang, M.; Chang, S.; Wu, X. G.; Zhang, X.; Tang, J.; Wang, M.; Ali, S.; Li, X.; Yu, G.; Han, J.; Wang, L.; Zou, B.; Zhong, H. Efficient Light-Emitting Diodes Based on in Situ Fabricated $FAPbBr_3$ Nanocrystals: The Enhancing Role of the Ligand-Assisted Reprecipitation Process. *ACS Nano* **2018**, *12* (8), 8808–8816. https://doi.org/10.1021/acsnano.8b05172.

(34) de Mello, J. C.; Wittmann, H. F.; Friend, R. H. An Improved Experimental Determination of External Photoluminescence Quantum Efficiency. *Adv. Mater.* **1997**, *9* (3), 230–232. https://doi.org/10.1002/adma.19970090308.

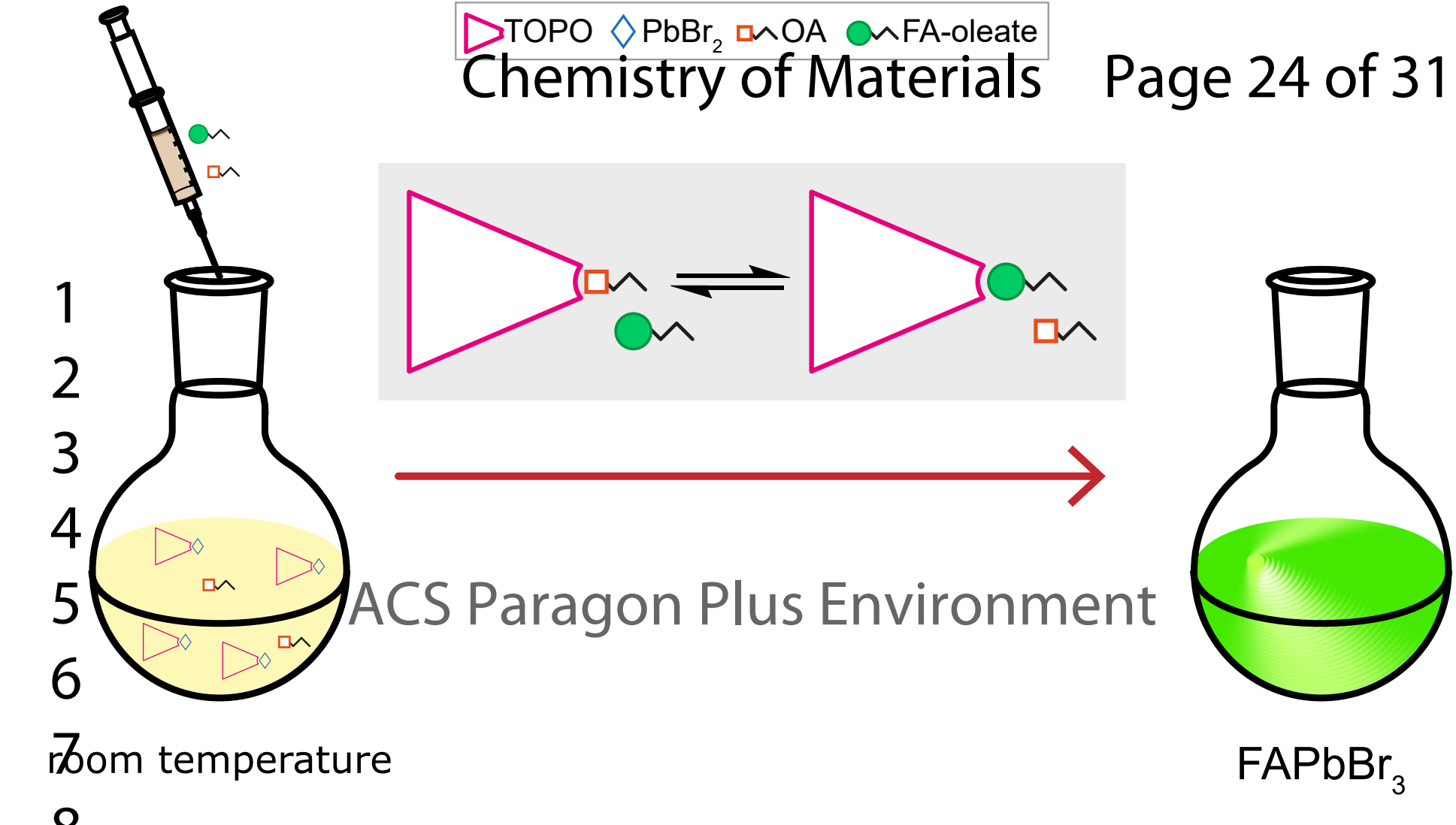
TOPO
PbBr2
OA
FA-oleate
ACS Paragon Plus Environment
room temperature
FAPbBr3

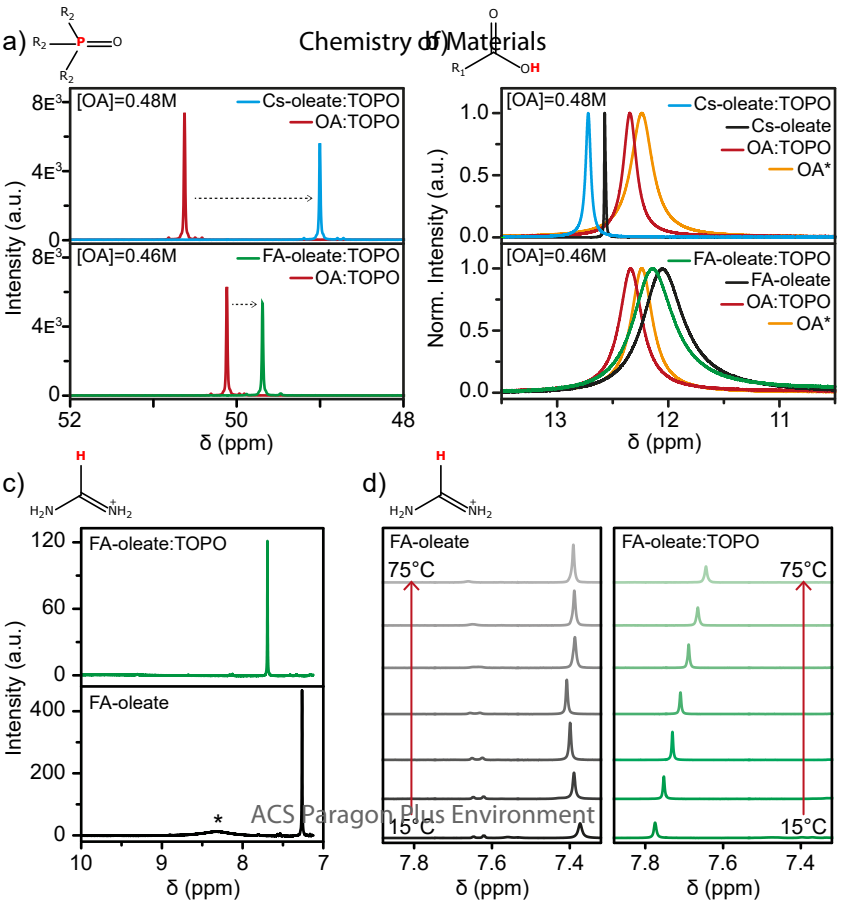
a)
b)
c)
d)
[OA]=0.48M
Cs-oleate:TOPO
OA:TOPO
[OA]=0.46M
FA-oleate:TOPO
Intensity (a.u.)
δ (ppm)
Cs-oleate
OA*
Norm. Intensity (a.u.)
FA-oleate
FA-oleate
75°C
15°C
ACS Paragon Plus Environment

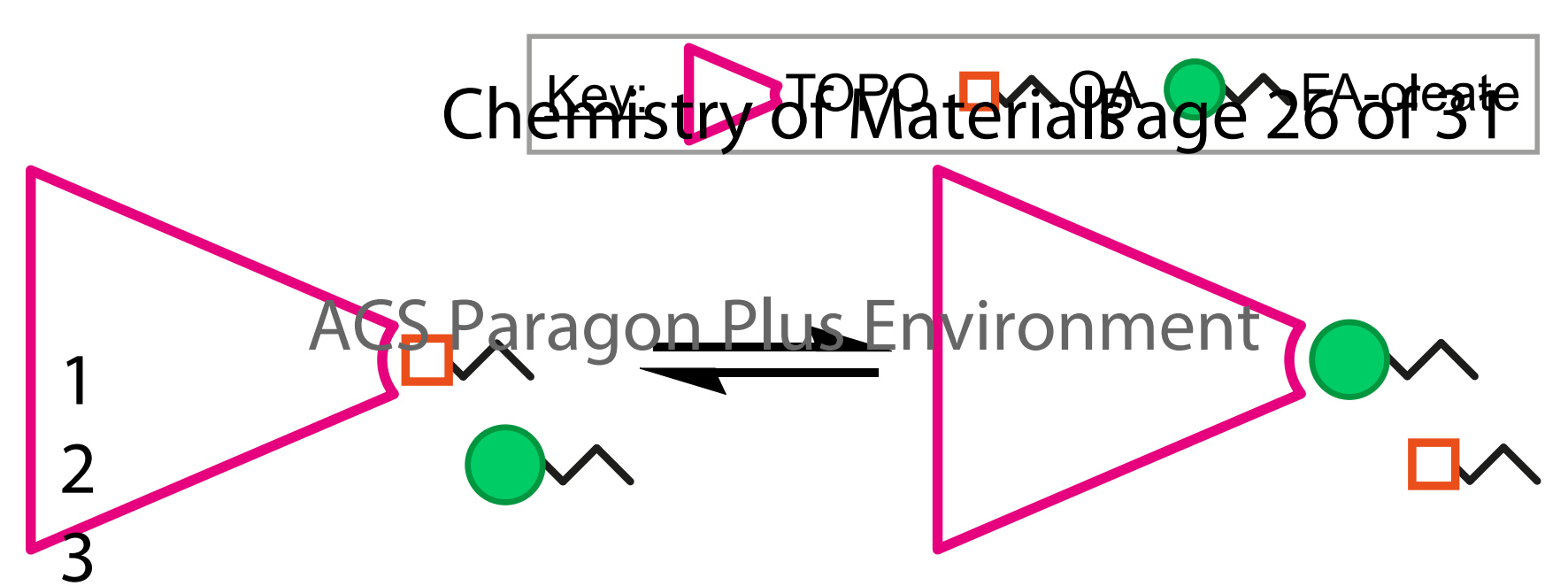
Key:
TOPO
OA
OA
EA-oleate
ACS Paragon Plus Environment
1
2
3